

Gamma-ray Diagnostics of *r*-process Nucleosynthesis in the Remnants of Galactic Binary Neutron-Star Mergers

YUKIKATSU TERADA,^{1,2} YUYA MIWA,¹ HAYATO OHSUMI,¹ SHIN-ICHIRO FUJIMOTO,³ SATORU KATSUDA,¹ AYA BAMBA,^{4,5} AND RYO YAMAZAKI^{6,7}

¹*Graduate School of Science and Engineering, Saitama University, 255 Sakura-ku, Saitama-shi, Saitama 338-8570, Japan*

²*Institute of Space and Astronautical Science, Japan Aerospace Exploration Agency, Sagami-hara, Kanagawa, Japan*

³*National Institute of Technology Kumamoto College, Kumamoto 861-1102, Japan*

⁴*Department of Physics, The University of Tokyo, 7-3-1 Hongo, Bunkyo, Tokyo 113-0033, Japan*

⁵*Research Center for the Early Universe, School of Science, The University of Tokyo, 7-3-1 Hongo, Bunkyo, Tokyo 113-0033, Japan*

⁶*Department of Physical Sciences, Aoyama Gakuin University, 5-10-1 Fuchinobe, Sagami-hara, Kanagawa 252-5258, Japan*

⁷*Institute of Laser Engineering, Osaka University, 2-6, Yamadaoka, Suita, Osaka 565-0871, Japan*

(Received Mar 03, 2022; Revised Apr 26, 2022; Accepted May 10, 2022)

Submitted to ApJ

ABSTRACT

We perform a full nuclear-network numerical calculation of the *r*-process nuclei in binary neutron-star mergers (NSMs), with the aim of estimating γ -ray emissions from the remnants of Galactic NSMs up to 10^6 years old. The nucleosynthesis calculation of 4,070 nuclei is adopted to provide the elemental composition ratios of nuclei with an electron fraction Y_e between 0.10 and 0.45. The decay processes of 3,237 unstable nuclei are simulated to extract the γ -ray spectra. As a result, the NSMs have different spectral color in γ -ray band from various other astronomical objects at less than 10^5 years old. In addition, we propose a new line-diagnostic method for Y_e that uses the line ratios of either $^{137\text{m}}\text{Ba}/^{85}\text{K}$ or $^{243}\text{Am}/^{60\text{m}}\text{Co}$, which become larger than unity for young and old *r*-process sites, respectively, with a low Y_e environment. From an estimation of the distance limit for γ -ray observations as a function of the age, the high sensitivity in the sub-MeV band, at approximately 10^{-9} photons $\text{s}^{-1} \text{cm}^{-2}$ or 10^{-15} erg $\text{s}^{-1} \text{cm}^{-2}$, is required to cover all the NSM remnants in our Galaxy if we assume that the population of NSMs by Wu et al. (2019). A γ -ray survey with sensitivities of 10^{-8} – 10^{-7} photons $\text{s}^{-1} \text{cm}^{-2}$ or 10^{-14} – 10^{-13} erg $\text{s}^{-1} \text{cm}^{-2}$ in the 70–4000 keV band is expected to find emissions from at least one NSM remnant under the assumption of NSM rate of 30 Myr^{-1} . The feasibility of γ -ray missions to observe Galactic NSMs are also studied.

Keywords: nuclear reactions, nucleosynthesis, abundances – gamma rays: general – gravitational waves

1. INTRODUCTION

Elements heavier than Bi exist in our universe, but their origin remains a mystery. Most cosmic isotopes heavier than the iron group are expected to be created by the rapid-neutron capture process, also known as the *r*-process (Cameron 1957; Burbidge et al. 1957; Cowan et al. 1991; Wanajo & Ishimaru 2006; Qian & Wasserburg 2007; Arnould et al. 2007), but the

actual nucleosynthesis sites capable of achieving such neutron-rich environments remains a matter of debate. Before the discovery of binary neutron-star mergers (NSM) observed as gravitational-wave objects like GW170817 (Abbott et al. 2017), NSMs were considered to be more promising as *r*-process nucleosynthesis sites than other primary candidates, such as core-collapse supernovae (SNe), because NSMs could achieve more neutron-rich (lower electron fraction Y_e) environments (Wanajo et al. 2011; Lattimer & Schramm 1974; Metzger et al. 2010). The event rate of NSMs is much lower than that of SNe, but the yield of *r*-process nuclei

in one event is expected to be very high (Wallner et al. 2015; Hotokezaka et al. 2015). Observational evidence of the existence of r -process nuclei has already been obtained by infrared observations of kilonovae (also called macronovae or r -process novae) in some short gamma-ray bursts, such as GRB 130603B (Tanvir et al. 2013) and the gravitational wave event GW170817 (Villar et al. 2017). However, the infrared radiation from NSMs is, in principle, the result of indirect emissions from unstable r -process nuclei, and any hint of elements heavier than the lanthanoids is still missing from the infrared information. Given that the nuclear levels of nuclei are in the MeV energy range, the γ rays from r -process nuclei should be the best probe for searching for r -process sites in the universe.

According to theoretical estimates of the γ -ray flux from binary NSMs (Hotokezaka et al. 2016), the γ -ray radiation immediately following a merging event is very dim at about 10^{-8} – 10^{-7} photons $\text{s}^{-1} \text{cm}^{-2} \text{keV}^{-1}$, even at an extremely close distance d of 3 Mpc. This flux is comparable with or below what the sensitivities of current and near-future MeV missions can detect. The precise measurements of photon energies are, in principle, rather difficult in the MeV band, where Compton scattering dominates over the photon-absorption process. Therefore, the ability to detect γ rays from NSMs by an immediate follow-up observation (a Target-of-opportunity observation; ToO) would be limited by the sensitivity of the γ -ray instruments. Instead, a non-ToO observation of γ rays from long-lived nuclei in NSMs would be an alternative way to survey r -process sites, and this has been proposed by Wu et al. (2019) and Wang et al. (2020). The γ -ray luminosity from nuclei with long lifetimes, on the order of 10^3 – 10^6 years, becomes much lower than that from short-lived nuclei, but if we limit the survey area within our Galaxy ($d \lesssim 10$ kpc), then the γ -ray flux in non-ToO observations is expected to become comparable with what is required for ToO observations. Therefore, non-ToO observations should provide more sensitive γ -ray surveys of NSMs, because the exposure time (the accumulation time of signals) is not limited like it is in ToO observations. Another benefit from performing a non-ToO survey is the better identification of γ -ray lines; we expect the effect of Doppler broadening to be smaller for older NSM remnants than for very young NSMs.

Here we focus on the non-ToO survey of γ rays from r -process nuclei in a possible Galactic NSM remnant. In this paper, we estimate γ -ray emissions from Galactic NSM remnants in an older age range than in previous work (Hotokezaka et al. 2016; Wang et al. 2020) by using nuclear-network numerical calculations with a

complete nuclear database. This paper also aims to provide γ -ray diagnostic methods for NSMs, showing the required sensitivities for future γ -ray observatories. In our study, we assume that the γ -ray instruments have a wider field-of-view (FOV) than the object size of the NSM remnants, which are larger than early NSMs in a ToO observation. We also assume that the instruments accumulate all of the γ -ray emissions from the NSM remnants, even though the nuclei may mix with the circumstellar medium (CSM) during the evolution of the remnants.

The rest of this paper is organized as follows. In Section 2, we summarize our environments and procedures for the nuclear-network numerical calculation and show the results for γ -ray emissions from NSM remnants. In Section 3, we present the γ -ray diagnostics that utilize spectral color to identify NSM remnants and provide the line properties for estimating the age t and Y_e . In Section 4, we discuss the survey distance and coverage in our Galaxy permitted by the instrument sensitivities, the corresponding limitation of the NSM rate in our Galaxy, and expectations for future missions.

2. NUMERICAL ESTIMATION OF GAMMA RAYS FROM NEUTRON-STAR MERGER REMNANTS

2.1. Overview of Numerical Calculation

To estimate the γ -ray emissions from binary NSM remnants of various ages, we performed a numerical simulation comprising the following three steps: **1)** calculation of the mass distribution of r -process nuclei for NSMs at $t = 1$ year, **2)** calculation of the decay processes of unstable nuclei emitting γ rays, and **3)** a simple calculation of the radiation transfer of γ rays from NSMs.

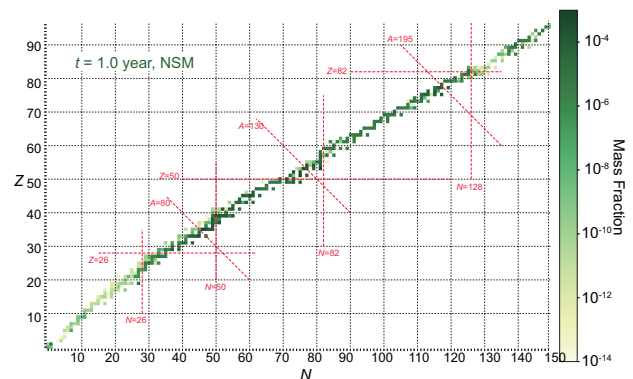


Figure 1. The r -process nuclei in the NSM case at $t = 1.0$ year on the table of nuclides. The magic numbers for neutrons and protons are indicated by red dashed lines

For the first step, we adopted the nucleosynthesis calculation for around 4,070 nuclei performed by

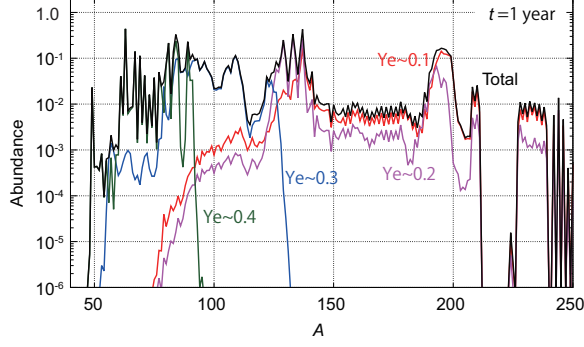


Figure 2. Mass number distribution of the abundance for the NSM case at $t = 1.0$ year, with $Y_e \sim 0.1, 0.2, 0.3$, and 0.4 , shown in red, magenta, blue, and green, respectively.

Fujimoto et al. (2007), which was cooled using the adiabatic expansion modeled from Freiburghaus et al. (1999) to provide the elemental composition ratios of nuclei for $Y_e = 0.10, 0.15, 0.20, 0.25, 0.30, 0.35, 0.40$, and 0.45 . This estimation assumes that the initial environment has a temperature of 9×10^9 K, radius of 100 km, entropy per baryon of $10k_B$, where k_B is the Boltzmann constant, and velocity of 2×10^9 cm s $^{-1}$, along with the initial abundances of the 4,070 nuclei in nuclear statistical equilibrium. As a result, the calculation provides the mass fractions at $t = 1$ year evaluated with the nuclear reaction network (network A in Fujimoto et al. 2007), by using $Y_e = 0.10$ – 0.45 in steps of 0.05. To set up the mass distribution of nuclei for the NSMs at $t = 1$ year, we blended the nuclei with the mass fraction using the Y_e provided in Wanajo et al. (2014). Specifically, the fractions are 4.54%, 4.85%, 14.6%, 29.7%, 10.3%, 25.1%, 10.5%, and 0.33% for $Y_e = 0.10, 0.15, 0.20, 0.25, 0.30, 0.35, 0.40$, and 0.45 , respectively. Note that this Y_e -fraction model by Wanajo et al. (2014) describes slightly-less neutron-rich environment than those by the recent dynamical-ejecta models after the kilonova observations of the gravitational event GW170817, such as four models in Kullmann et al. (2022) under two kinds of equation-of-states, density dependent 2 (DD2) (Hempel & Schaffner-Bielich 2010; Typel et al. 2010) and SFHo (Steiner et al. 2013). In this paper, we adopted the first one by Wanajo et al. (2014) as a pessimistic case for the r -process site, but changing the Y_e -fraction models does not change the conclusions from the γ -ray spectra as tested in the later section 3. Figure 1 shows the mass fraction of multiple nuclei at $t = 1$ year generated in an NSM case, information that is given in the table of nuclides (neutron number N vs atomic number Z). Using the same data set, Figure 2 summarizes the distribution of nuclei with mass number A at $t = 1$ year, showing the contributions of Y_e .

This plot demonstrates that the environment with lower Y_e contributes to the generation of heavier elements.

For the second step, we simulated the decay processes of unstable nuclei, starting from the mass distribution at $t = 1$ year calculated in the first step. We used the Decay Data File 2015 (DDF-2015) (Katakura & Minato 2016) in the Japanese Evaluated Nuclear Data Library (JENDL) (Katakura 2012), which provides the decay profiles of 3,237 nuclei up to $Z=104$ (Rf). Here we applied a correction to the γ -ray information for ^{241}Am ; this error was reported from our study and was fixed in the next version of the database. The originality of this study lies in the comprehensiveness of nuclei treated in the calculation. In the nuclear-decay calculation, we adopted the α -decay, β^- -decay, β^+ -decay, electron capture, isomeric transition, and γ -decay processes. In our calculation, the internal conversion process is ignored, which emits soft X-rays and makes a negligible contribution to the γ -ray band. The neutron- and proton-emission processes are also ignored because they contribute to the very early phase, which is out of the scope of this study. The spontaneous fission process may occur on ^{257}Es , ^{256}Cf , ^{254}Cf , and ^{250}Cm , but its contribution is negligible. Thus, this process is also excluded from our calculation. In addition, we do not calculate the γ -ray emission from secondary electrons (electrons from β -decay, δ -rays, and so on) after the decay of unstable nuclei.

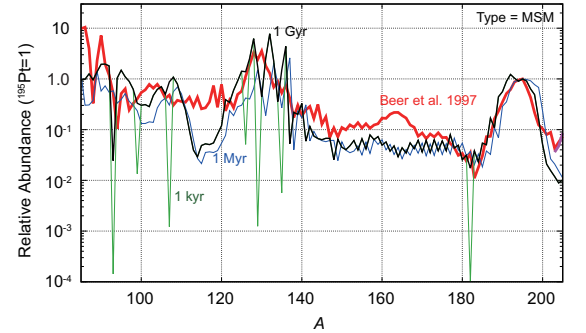


Figure 3. The relative abundance of ^{195}Pt in the NSM case at $t = 1$ thousand, 1 million, and 1 billion years, shown in green, blue, and thick black, respectively, compared with the semi-empirical abundance distribution of Beer et al. (1997).

To verify the calculations in the second step, we refer to Figure 3, which represents the relative abundances of nuclei at $t = 1$ thousand, 1 million, and 1 billion years as a function of A . The distribution in A does not change dramatically after $t \sim 1$ thousand years, except for the disappearance of the small dips at the magic numbers. The distribution for $t > 1$ million years becomes roughly consistent with the semi-empirical abundance distribu-

tion of cosmic r -process nuclei in Beer et al. (1997), which is close to the solar abundance distribution.

For the outputs of the second step, we obtain the γ -ray flux $F_{\gamma,i}$ from the NSM at distance d . Using the nuclear γ -ray intensity $I_{\gamma,i}$ of the i -th element with the mass number A_i , the mass M_i , and the half-life $T_{1/2}$, the $F_{\gamma,i}$ in a small time interval dt is described as

$$F_{\gamma,i} = \frac{N_A}{4\pi d} \frac{M_i}{A_i} \frac{I_{\gamma,i}}{T_{1/2}} \left(\frac{1}{2}\right)^{-dt/T_{1/2}}, \quad (1)$$

where N_A is Avogadro's number.

Finally, the third step is to calculate the transfer of γ rays through the NSM ejecta. However, we omitted the detailed Monte-Carlo calculation of the radiation transfer because the optical depth decreases rapidly after the merger event, by roughly $\propto \sqrt{t}$ (Li 2019); within the scope of our study at $t \gg 1$ year, the optical depth is thin and negligible. Therefore, the degradation of the line profiles by Compton scattering is not included in our calculation, which would be dominant in only the very early phase. Note that the detail calculations of the MeV γ -ray spectra from Galactic NSMs in the initial phase were performed by Wang et al. (2020); ?. In this step, we apply only the bulk Doppler-broadening effect caused by the expansion velocity $v(t)$. The thermal Doppler-broadening effect is ignored in this calculation because it is two or three orders of magnitude smaller than that from the expansion motion of the heavy elements in the $A = 50$ –200 range. In reality, the line profile from the bulk Doppler effect becomes complicated due to the complex contributions of various velocity components, as has been observed in the X-ray lines from heavy elements in SN remnants (Grefenstette et al. 2017; Kasuga et al. 2018). For simplicity, we applied the Gaussian distribution function for the line profile in the calculation. Of the various velocity elements in the remnant, we applied only single Gaussian broadening to the maximum velocity component, which we assume to be the forward shock motion. This was done to simulate the most robust case for considering the γ -ray sensitivity. In our assumption, $v(t)$ starts from the initial value $v(0) = 0.3 c$, where c is the speed of light, and evolves at a constant rate during the free expansion phase. During the Sedov-Taylor phase, $v(t)$ evolves as $v(t) \propto t^{-(3/5)}$ (Taylor 1950), and then as $v(t) \propto t^{-(0.7)}$ during the pressure-driven snowplow (PDS) phase (McKee & Ostriker 1977). We assume that the free expansion, Sedov-Taylor, and PDF phases end at $t = 10$, 4.7×10^4 , and 1.65×10^6 years, respectively. The ages of these phase transitions may change by about one order of magnitude due to differences in density of the CSM, but this modification affects only the Doppler-

broadening effect. It becomes negligible when compared with the typical energy resolutions of γ -ray instruments for ages older than $t \sim 1,000$ years, the range that lies within the scope of this study. Note that even at $t = 10^6$ years, $v(t)$ approaches $\sim 20 \text{ km s}^{-1}$, which is about double the speed of sound for a typical CSM density of 0.01 cm^{-3} . The radius becomes $\sim 100 \text{ pc}$. Finally, we get the γ -ray spectra for NSMs at t , accumulated from all of the r -process nuclei in the ejecta.

2.2. Gamma-ray Emission and Evolution

From the numerical calculation described in Section 2.1, the γ -ray spectra from $t = 3$ to 1 million years, under the assumption that the ejecta mass is $M_{\text{ej}} = 0.01 M_{\odot}$ at $d = 10 \text{ kpc}$, are summarized in Figures 4 and 5. As described in Section 1, we assume that all of the emissions from the NSM remnants are observable within the wider FOV; this is assumed to be larger than the object size, which becomes around 10 pc at $t = 1,000$ years and expands into around 100 pc at $t > 10^6$ years. The spectra contain many nuclear lines broadened by the Doppler effect. They appear to form a continuous spectrum in the early phase, but they become separated at ages older than 1,000 years. Note that the γ -ray data without the Doppler-broadening effect (the outputs from the second step of the calculation in Section 2.1) is provided as the numerical model for the XSPEC tool (Arnaud 1996) in the HEAsoft package (Appendix A).

To identify the γ -lines in the spectra, we checked the most prominent lines in the γ -ray spectra generated by a single Y_e condition. Table 1 lists the brightest lines shown for the nuclei in each Y_e . Roughly speaking, the bright lines seen for objects of a younger age lie in the higher-energy γ -ray band of the spectrum. Further details of the diagnostics will be discussed in Section 3.

3. GAMMA-RAY DIAGNOSTICS OF NEUTRON-STAR MERGER REMNANTS

3.1. Spectral Color Changes of Neutron-Star Merger Remnants

Using the energy spectra of the NSM remnants (Figures 4 and 5), we first checked the properties of the spectral shapes from the hard X-ray to the soft γ -ray bands. As shown in the normalized spectra plotted in Figure 6, the energy spectra roughly evolve from hard to soft slopes. γ -ray emission decreases rapidly leaving the hard X-ray emission in old age, as is indicated in Table 1. This phenomenon of γ rays is equivalent to the Sargent law for β decay.

To see the evolution of the shape of the γ -ray spectra more quantitatively, we plotted the light curves of the γ -ray flux in three bands: 70 to 200 keV, 200 to 500 keV,

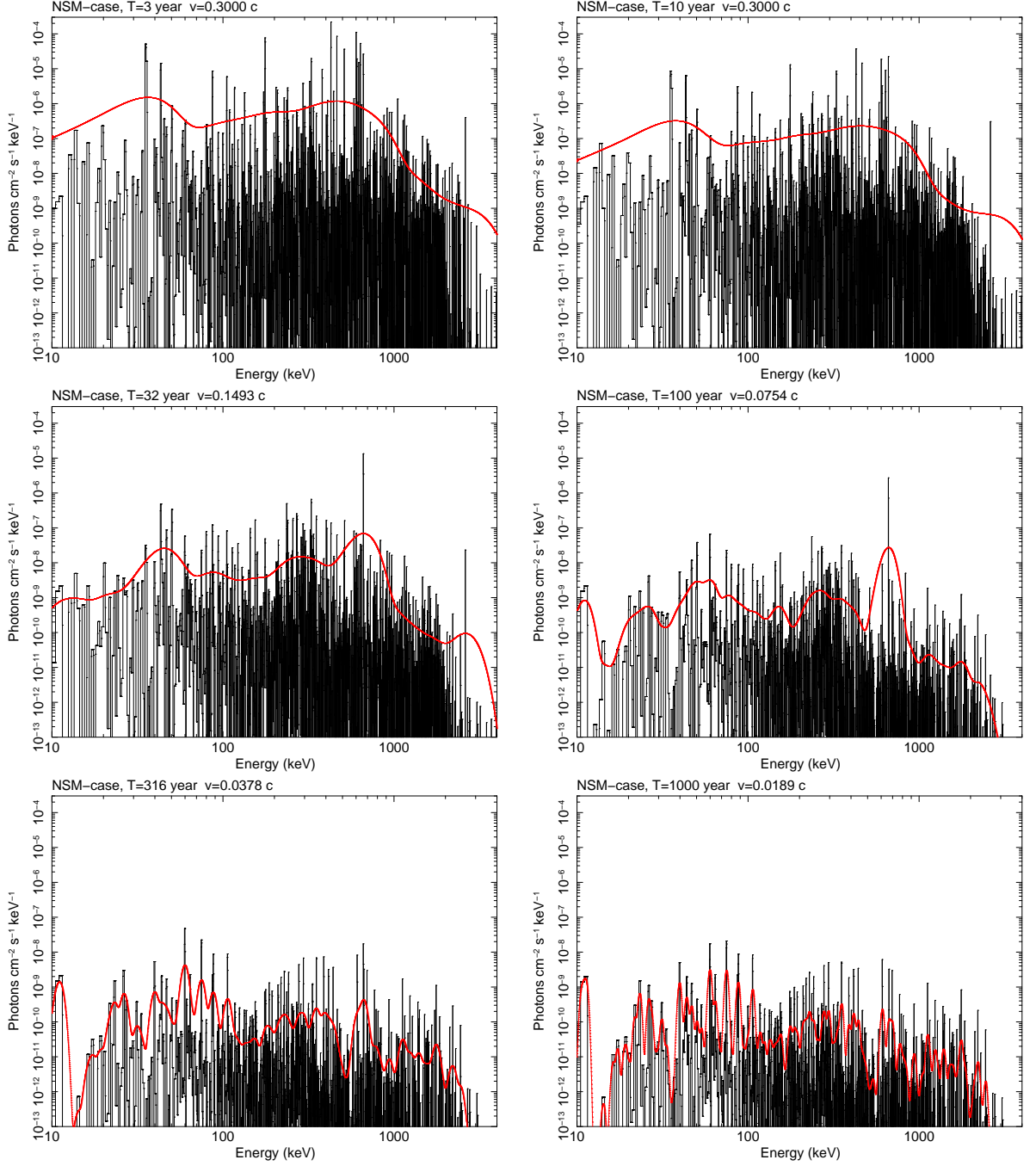


Figure 4. Gamma-ray spectra simulated for the NSM case at $t = 3 - 1,000$ years, assuming a distance of 10 kpc with an initial velocity of $0.3 c$ (see the text). The red and black plots represent the spectra with and without the Doppler-broadening effect, respectively. The time since the merging event and the velocities are shown in each top label.

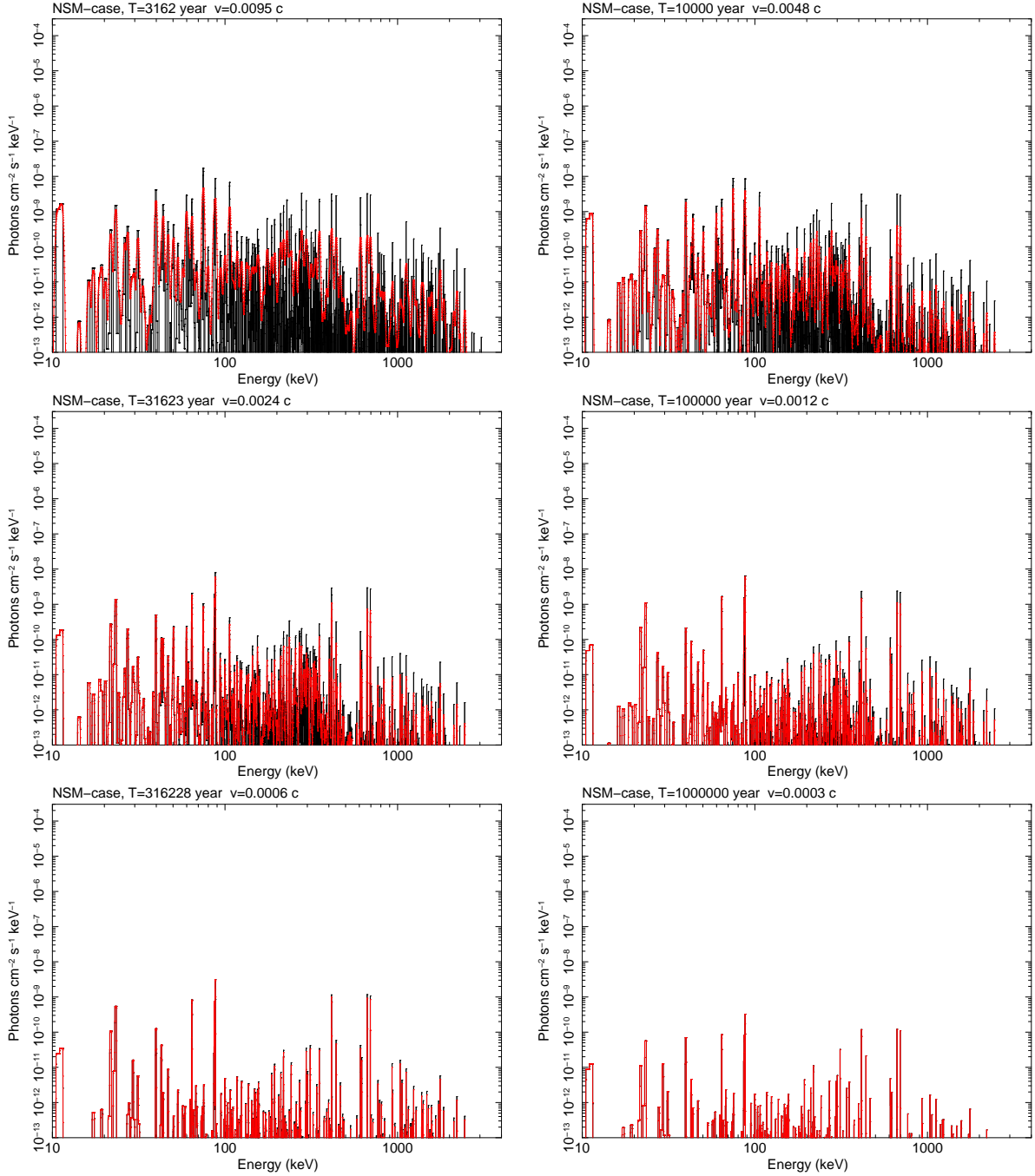


Figure 5. Same as Figure 4 but for $t = 3,162$ – $1,000,000$ years.

and 500 to 3,000 keV, which cover multiple lines around 100 keV and 300 keV, and a prominent line around 700 keV, respectively. As indicated in the top panel of Figure 7, the flux in the higher-energy bands decreases more quickly than that in the low-energy bands. A decaying trend is also seen in the time dependency of the hardness ratio among these bands, as is indicated in the lower panel of Figure 7. The ratio drops dramatically at around 200–300 years, indicating that the γ -ray flux

above the 500 keV band quickly decreases at this age. This phenomenon is primarily due to the decay of ^{125}Sb and $^{137\text{m}}\text{Ba}$ listed in Table 1. Note that this result does not change even if we adopt other Y_e -fraction models of DD2-125145, DD2-135135, SFHo-125145, and SFHo-135135 in Kullmann et al. (2022), as shown in Figure 7.

To compare the spectral shape of NSM remnants with other astronomical objects, we plotted the color-color di-

Energy (keV)	Nuclei	Major Y_e	Half-life
40.0 ‡	^{225}Ra	0.10–0.20	$\sim 7.9 \times 10^3$ yr, 1.6×10^5 yr, 2.1×10^8 yr
58.6 ‡	$^{60\text{m}}\text{Co}$	0.35–0.40	$\sim 2.6 \times 10^6$ yr
59.5	^{241}Am	0.10–0.20	$\sim 4.3 \times 10^2$ yr, 8.4×10^3 yr
74.7 ‡	^{243}Am	0.15–0.20	$\sim 7.4 \times 10^3$ yr
87.6 †	^{126}Sn	0.10–0.30	$\sim 2.3 \times 10^5$ yr
106.1 ‡	^{239}Np	0.10–0.20	$\sim 4.5 \times 10^9$ yr
236.0	^{227}Th	0.10	~ 21 yr, 3.2×10^4 yr, 7.0×10^8 yr
276.0	^{81}Kr	0.45	$\sim 2.2 \times 10^5$ yr
311.9	^{233}Pa	0.10–0.20	$\sim 2.1 \times 10^6$ yr
328.4	^{194}Ir	0.10–0.15	~ 6 yr
427.9 †	^{125}Sb	0.25–0.30	~ 2.7 yr
440.5 ‡	^{213}Bi	0.10–0.20	$\sim 7.3 \times 10^3$ yr
511.9	^{106}Rh	0.30–0.35	~ 1.1 yr
513.9 †	^{85}Kr	0.30–0.40	~ 10 yr
561.1, 834.5	^{92}Nb	0.45	$\sim 3.4 \times 10^7$ yr
609.3 ‡	^{214}Bi	0.10–0.20	$\sim 1.6 \times 10^3$ yr, $\sim 7.5 \times 10^4$ yr
661.7 †	$^{137\text{m}}\text{Ba}$	0.10–0.25	~ 30 yr
765.8	^{95}Nb	0.30–0.35	~ 34 d, 64 d
871.1, 702.6	^{94}Nb	0.45	$\sim 2.0 \times 10^4$ yr
1115.5	^{65}Zn	0.45	~ 243 d
1157.0	^{44}Sc	0.45	~ 60 yr
1332.5	^{60}Co	0.45	~ 5.2 yr

Table 1. List of nuclei and their most prominent nuclear γ -ray lines, arranged by Y_e . The † and ‡ marks indicate the lines used in the Y_e diagnostics in Section 3.3 for young ($t < 100$ years) and old ($t > 100$ years) cases, respectively. Note that the 'm' in $^{137\text{m}}\text{Ba}$ indicates that it is meta-stable.

agrams in the hard X-ray band (10–500 keV) and in the hard X-ray to γ -ray band (70–3000 keV), in the top and bottom of Figure 8, respectively. We divided the energy band-pass for these spectra into three ranges: 10–25, 25–70, and 70–500 keV for the hard X-ray band (top of Figure 8), and 70–500, 500–1,000, and 1,000–3,000 keV for the hard X-ray to γ -ray band (Figure 8 bottom). Note that the divisions of the energy bands are defined so that they follow the energy band-pass of current γ -ray instruments on board NuSTAR (Harrison et al. 2013), INTEGRAL (Winkler et al. 2003), and other observatories. For comparison, the spectral colors of other astronomical objects, calculated using the INTEGRAL

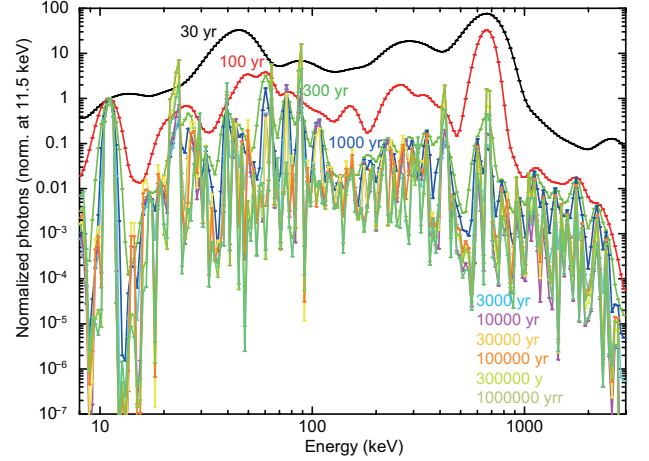


Figure 6. The energy spectra with Doppler broadening, same as the red plots in Figures 4 and 5 but normalized to the 11.5 keV flux at 30, 100, 300, 1000, 3000, 10000, 30000, 100000, 300000, and 1000000 years, which are shown in black, red, green, blue, light blue, magenta, yellow, orange, yellow green, and olive green, respectively.

catalog version 0043¹, are also plotted in the same figures. In the hard X-ray band (the 10–500 keV band in the top of Figure 8), the spectra of NSM remnants older than $t \sim 1,000$ years have spectral colors similar to those of supernova remnants or active galactic nuclei, but NSM remnants younger than $t \sim 1,000$ years can be distinguished from other known objects by their hard X-ray colors. In other words, the spectral color in the hard X-ray band below 500 keV is a good indicator of young NSM remnants. Furthermore, this differentiation from known objects becomes more prominent when we include the higher-energy band covering the MeV portion of the spectrum, as is clearly indicated in the bottom of Figure 8. Note that this result does not change even if we adopt other Y_e -fraction models of DD2-125145, DD2-135135, SFHo-125145, and SFHo-135135 in Kullmann et al. (2022), as shown in Figure 8. Therefore, NSM remnants have unique spectral colors in the hard X-ray to γ -ray bands. This observation is one of the important conclusions from our calculation. Note that the spectral models in the INTEGRAL catalog are simple enough that the colors of known objects in the gamma-ray band (bottom of Figure 8) are less scattered than those in the hard X-ray band (top of Figure 8). The spectral separation between NSM remnants and other objects in the bottom of Figure 8 does not change dramatically, even if we lower the low-energy threshold (70 keV in the bottom of Figure 8) to cover 20

¹ <https://www.isdc.unige.ch/integral/science/catalogue>

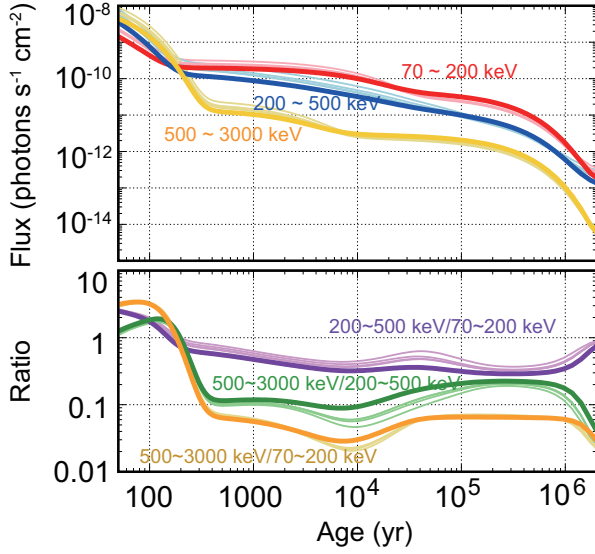


Figure 7. The top panel represents the light curve of the γ -ray spectra simulated for the case of an NSM at a distance of 10 kpc, with the Doppler-broadening effect and an initial velocity of $0.3 c$. The energy bands of 70–200 keV, 200–500 keV, and 500–3000 keV, are shown in red, blue, and yellow, respectively. The bottom panel represents the ratios among the three bands in the top panel: the ratio between the 70–200 keV and 200–500 keV bands, that between the 200–500 keV and 500–3000 keV bands, and that between the 70–200 keV and 500–3000 keV bands are shown in purple, green, and orange, respectively. The dim colors represent the results using the Y_e -fraction by Wanao et al. (2014) as the nominal condition of this paper, and the lighter color lines represent the results by the other models, DD2-125145, DD2-135135, SFHo-125145, and SFHo-135135 in Kullmann et al. (2022).

keV, for example. However, it becomes worse if we set it higher so that everything up to a certain point, 200 keV, for example, is ignored. This implies that hard X-rays around 100 keV provide the key information for distinguishing NSM remnants from other objects. Note that these results are based on the pure-nuclear γ rays from r -process nuclei in NSMs, and thus the synchrotron radiation from electrons that are accelerated by the shocks may contaminate the hard X-ray band for young remnants. Additionally, when taking actual observations, we must be careful to isolate the contamination of the hard X-ray spectrum that arises from other objects located behind the NSM, such as active galactic nuclei within the FOV.

3.2. Nuclear Line Emissions from Older Neutron-Star Merger Remnants

For ages older than $t > 3,000$ years, nuclear lines are clearly seen in the γ -ray spectra of NSM remnants due to the minimal Doppler-broadening effect, as is shown in Figures 4 and 5. Using the γ -ray spectra of NSM

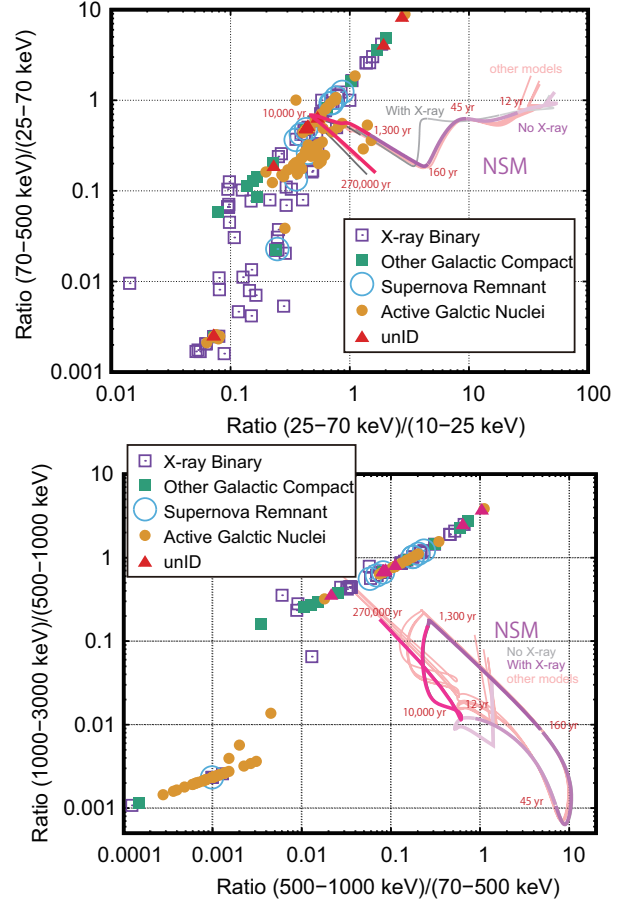


Figure 8. (Top) A color-color diagram of the flux ratio between the 10–25 keV and 25–70 keV bands versus that between the 25–70 keV and 70–500 keV bands is shown using simulated γ -ray spectra for the case of an NSM at a distance of 10 kpc, with the Doppler-broadening effect and an initial velocity of $0.3 c$. The spectral evaluations of the NSM both with and without K X-ray emission are shown by magenta and gray lines, respectively, and those by the other Y_e -fraction models, DD2-125145, DD2-135135, SFHo-125145, and SFHo-135135 in Kullmann et al. (2022), are shown in the light-pink lines, for reference. The color-color diagram of the X-ray objects listed in the INTEGRAL catalog (version 0043) are also plotted: X-ray binaries with the purple squares, galactic compact objects, such as cataclysmic variables, with the green squares, supernova remnants with the cyan circles, active galactic nuclei with the orange circles, and unidentified objects with the red triangles. (Bottom) Same plot as the top panel but in the 70–500, 500–1,000, and 1,000–3,000 keV bands.

remnants that were shown in Section 2 (i.e., the Y_e distribution for the NSM case with $M_{\text{ej}} = 0.01 M_\odot$ at $d = 10$ kpc), we selected the brightest nuclear lines in each energy band, 3–75 keV, 75–500 keV, and 500–4000 keV, for at least one epoch in the age range spanning $t = 10$ to 4×10^6 years. Note that these energy bands are defined in such that they simulate

the energy bands that are observable by current and near-future instruments aboard satellites, such as the hard X-ray focusing missions NuSTAR (Harrison et al. 2013) and FORCE (Nakazawa et al. 2018), and γ -ray missions like INTEGRAL (Winkler et al. 2003), e-ASTROGAM (De Angelis et al. 2017; de Angelis et al. 2018), AMEGO (Kierans 2020), and GRAMS (Aramaki et al. 2020).

Figure 9 presents the time evolution of the brightest nuclear γ -ray lines in these energy bands. To account for the reduction in the line sensitivities as a result of the Doppler-broadening effect, we accumulated the photons that were within the energy resolution of $\Delta E = 3 \pm 1$ keV from the center energy of their associated lines. This chosen value for the energy resolution is typical for semiconductor γ -ray detectors. For reference, the evolution of lines without Doppler broadening is also shown in the figure as dashed lines. As indicated in Figure 9, the Doppler-broadening effect becomes less dominant in the hard X-ray band after a few hundred years, but it is still present until about $t = 10^3$ and 10^4 years in the soft γ -ray and the hard γ -ray bands, respectively. Note that the reason why several lines, such as those of ^{126m}Sb and ^{239}Np , increase as t approaches 10^3 – 10^5 years is that the number of parent nuclei increases in these phases.

From Figure 9, we can identify the nuclear lines that are useful as indicators for the ages of NSMs. The ages can be categorized into three epochs: $t < 100$ years, $t \sim 10^3$ – 10^4 years, and $t > 10^4$ years. In summary, if we detect the lines from ^{125}Sb , ^{194}Os , ^{227}Th , or ^{194}Ir , then we can determine the age of the NSM to be very young at $t < 100$ years. Similarly, lines from ^{137m}Ba in the γ -ray band indicate that the age is around $t \sim 10^2$ years. In the age range spanning $t \sim 10^3$ – 10^4 years, nuclear lines will be detected from ^{241}Am , ^{243}Am , ^{214}Pb , ^{239}Np , and/or ^{214}Bi . A nuclear line from ^{126m}Sb indicates that the NSM is very old at $t > 10^4$ years. In the wide age range from $t = 400$ to 10^5 years, the line from ^{126}Sn stays almost constant at 10^{-9} photons $\text{s}^{-1} \text{cm}^{-2}$ for a distance of $d = 10$ kpc, and thus it can be used as a standard candle for measuring d .

3.3. Line Diagnostics for the electron fraction

In addition to the spectral colors (Section 3.1), nuclear lines can be used to identify NSM remnants among astronomical objects, especially when the remnants are of an older age. Since the NSMs are thought to have both a more neutron-rich environment and a lower Y_e condition than SNs (Wanajo et al. 2011; Lattimer & Schramm 1974; Metzger et al. 2010), a new line-diagnostic method utilizing Y_e values will be useful for distinguishing NSMs from SNe. In this subsection, we search for γ -ray line di-

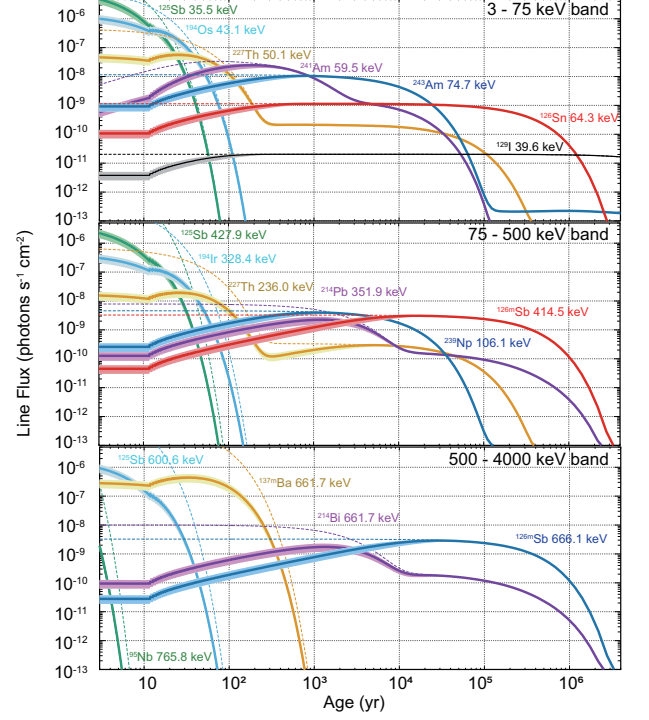


Figure 9. The time evolution of the brightest γ -ray lines in the energy bands of 3–75 keV, 75–500 keV, and 500–4000 keV are shown in the top, middle, and bottom panels, respectively. The line fluxes with and without the Doppler effect are shown as thick and dashed lines, respectively. The thick lines plot the γ -ray fluxes within the $\Delta E = 3$ keV width, and the upper and lower boundaries of the corresponding hatched areas show the flux within the $\Delta E = 2$ keV and 4 keV widths, respectively. The nuclei and energies are indicated by the same color as the lines and hatches.

agnostics for Y_e . We use the γ -ray spectra calculated under the pure Y_e conditions in the $Y_e = 0.10$ – 0.45 range, whereas in the previous sections we used the mixed Y_e condition for NSMs.

To identify the best candidates among the nuclear γ -ray lines for the identification of Y_e , we first selected the five brightest lines for each age, $t = 100, 1000, 10^4, 10^5$, and 10^6 years, and for each $Y_e (= 0.10, 0.15, 0.20, 0.25, 0.30, 0.35, 0.40, \text{ and } 0.45)$. Then among these 5 (ranks) \times 5 (t) \times 7 (Y_e) lines, we selected the nuclear lines which appeared in two or more of the conditions for t and Y_e . In total, ten γ -ray lines are selected and are marked as † and ‡ in Table 1 for $t < 100$ years and $t > 100$ years, respectively. Therefore, the lines from ^{137m}Ba (661.66 keV), ^{85}Kr (513.9 keV), and ^{125}Sb (427.87 keV) in ages below 100 years are indicators of low, middle, and high Y_e environments, respectively. Here, low, middle, and high are numerically defined as $Y_e \sim 0.10$ – 0.20 , 0.20 – 0.35 , and 0.35 – 0.45 , respectively. In ages older than $t = 100$ years, the lines from ^{225}Ra

(40.0 keV), ^{243}Am (74.66 keV), ^{239}Np (106.1 keV), ^{213}Bi (440.5 keV), and ^{214}Bi (609.3 keV) are emitted from a low Y_e environment, whereas the lines from $^{60\text{m}}\text{Co}$ (58.6 keV) and ^{126}Sn (87.6 keV) become bright in the middle and high Y_e environments, respectively.

Since the absolute flux of a single line changes with respect to t and d , the ratio between two or more lines should be a good indicator for Y_e . Figure 10 summarizes the line intensities and their ratios using the ten nuclei selected above. For simplicity, the plots for young and old ages, $t = 10\text{--}10^3$ years and $10^3\text{--}10^6$ years, respectively, are shown separately. In the young age range (top of Figure 10), the ratios of $^{137\text{m}}\text{Ba}/^{85}\text{Kr}$, $^{125}\text{Sb}/^{137\text{m}}\text{Ba}$, and $^{85}\text{Kr}/^{125}\text{Sb}$ become larger than unity in the low, middle, and high Y_e environments, respectively. These low and high Y_e indicators (i.e., $^{137\text{m}}\text{Ba}/^{85}\text{Kr}$ and $^{85}\text{Kr}/^{125}\text{Sb}$, respectively) exhibit more prominent ratios over time since ^{85}Kr decays slower than ^{125}Sb and faster than $^{137\text{m}}\text{Ba}$, whereas the middle indicator ($^{125}\text{Sb}/^{137\text{m}}\text{Ba}$) becomes dim after 100 years. Note that the plots use the incident line fluxes calculated in step 2 of Section 2.1, and the reduction due to the Doppler-broadening effect is not considered. The Doppler effect is particularly significant in plots for the young age range (top of Figure 10). Quantitatively, the ratios of $^{137\text{m}}\text{Ba}/^{85}\text{Kr}$, $^{125}\text{Sb}/^{137\text{m}}\text{Ba}$, and $^{85}\text{Kr}/^{125}\text{Sb}$ change by factors of 1.57, 0.82, and 0.77, respectively, for $t < 1,000$ years. In the old age range (middle of Figure 10), the ratios of $^{243}\text{Am}/^{60\text{m}}\text{Co}$, $^{126}\text{Sn}/^{243}\text{Am}$, and $^{60\text{m}}\text{Co}/^{126}\text{Sn}$ indicate the low, middle, and high Y_e environments, respectively. The line from ^{239}Np has the same flux and time evolution as that from ^{243}Am (red plots), because they are in the same decay chain. Similarly, the lines from ^{214}Bi , ^{225}Ra , and ^{213}Bi (green plots) follow almost the same trend as those from ^{243}Am and ^{239}Np (red plots). Among them, the low Y_e indicator ($^{243}\text{Am}/^{60\text{m}}\text{Co}$) in the old age range is valid up to $t = 1$ million years, and the middle Y_e indicator ($^{126}\text{Sn}/^{243}\text{Am}$) shows more significant ratios with $t > 10^3$ years. On the other hand, lines for the high Y_e indicator $^{60\text{m}}\text{Co}/^{126}\text{Sn}$ decay quickly and become unavailable after 10^3 years; that is, if the ratio $^{60\text{m}}\text{Co}/^{126}\text{Sn}$ is larger than unity, then the object is in a high Y_e environment with an age of $t \sim 10^3$ years. In summary, using these indicators, which become larger than unity in specific Y_e conditions, we can estimate the Y_e environment independently from the spectral-color diagnostics shown in Section 3.1.

Finally, we checked the line ratios blended by Y_e distributions of the NSM cases. The time evolution is plotted in Figure 10 bottom. The difference of the Y_e -fraction models between Wanajo et al. (2014) and

Kullmann et al. (2022) does not affect the trend of the NSMs so much. These γ -ray lines are also expected to be observed from the remnants of core-collapse SNe, which are considered to be less neutron-rich environment at $Y_e \sim 0.5$ (Andrews et al. 2020) than NSMs. However, our numerical-calculation model in this paper has limitations in estimating γ -ray radiation from the core-collapse SNe, because the mass fractions of the r -process nuclei in the ejecta are different between the maximum Y_e condition of our calculation (i.e., $Y_e = 0.45$) and the SNe case ($Y_e \sim 0.50$), and the neutron-rich nuclei in the nominal core-collapse SNe are predominantly generated via the s -process rather than the r -process. For reference, we plotted the time evolution of the line ratios in the γ -ray spectra of $Y_e = 0.45$, which should still reproduce well an environment with almost-equal numbers of neutrons and protons. According to Figure 10 bottom, we expect the low- Y_e indicators (i.e., $^{137\text{m}}\text{Ba}/^{85}\text{Kr}$ and $^{243}\text{Am}/^{60\text{m}}\text{Co}$) in the NSM case become many orders-of-magnitude larger than those in the SNe case. In the core-collapse SNe where neutron-rich nuclei are generated via the s -process, relatively large amount of ^{85}Kr and almost no ^{243}Am are synthesized. Therefore, the difference of these low- Y_e indicators between the NSMs and SNe cases are expected to become larger than Figure 10 bottom. As for the middle- Y_e indicators ($^{125}\text{Sb}/^{137\text{m}}\text{Ba}$ and $^{126}\text{Sn}/^{243}\text{Am}$), they may not be useful to distinguish γ -rays from NSMs and SNe according to Figure 10 bottom. In the s -process environment of core-collapse SNe, almost no $^{137\text{m}}\text{Ba}$ and ^{243}Am are synthesized and thus these middle- Y_e indicators can be larger than the values in the figure. Finally, the high- Y_e indicators ($^{85}\text{Kr}/^{125}\text{Sb}$ and $^{60\text{m}}\text{Co}/^{126}\text{Sn}$) can discard the NSMs from the SNe cases as indicated by Figure 10 bottom. In summary, the new line-diagnostic method for Y_e provides a tool for distinguishing between NSMs and SNe.

4. DISCUSSION

In Section 2, we presented a nuclear-decay simulation using a large nuclear database, the goal of which was to estimate the γ -ray spectra of NSMs up to the age of $t = 10^6$ years. We have identified many nuclear lines, listed in Table 1, that can be used for identifying the nucleosynthesis environments of NSMs, even with the Doppler-broadening effect altering the profiles of these lines in the young age range. In Section 3, we numerically analyzed the simulated γ -ray spectra from NSMs and found that the spectral slope in the soft γ -ray band above 500 keV changes at around $t = 200\text{--}300$ years. We also found that the spectral colors of NSMs in the hard X-ray to soft γ -ray bands differ from those of other

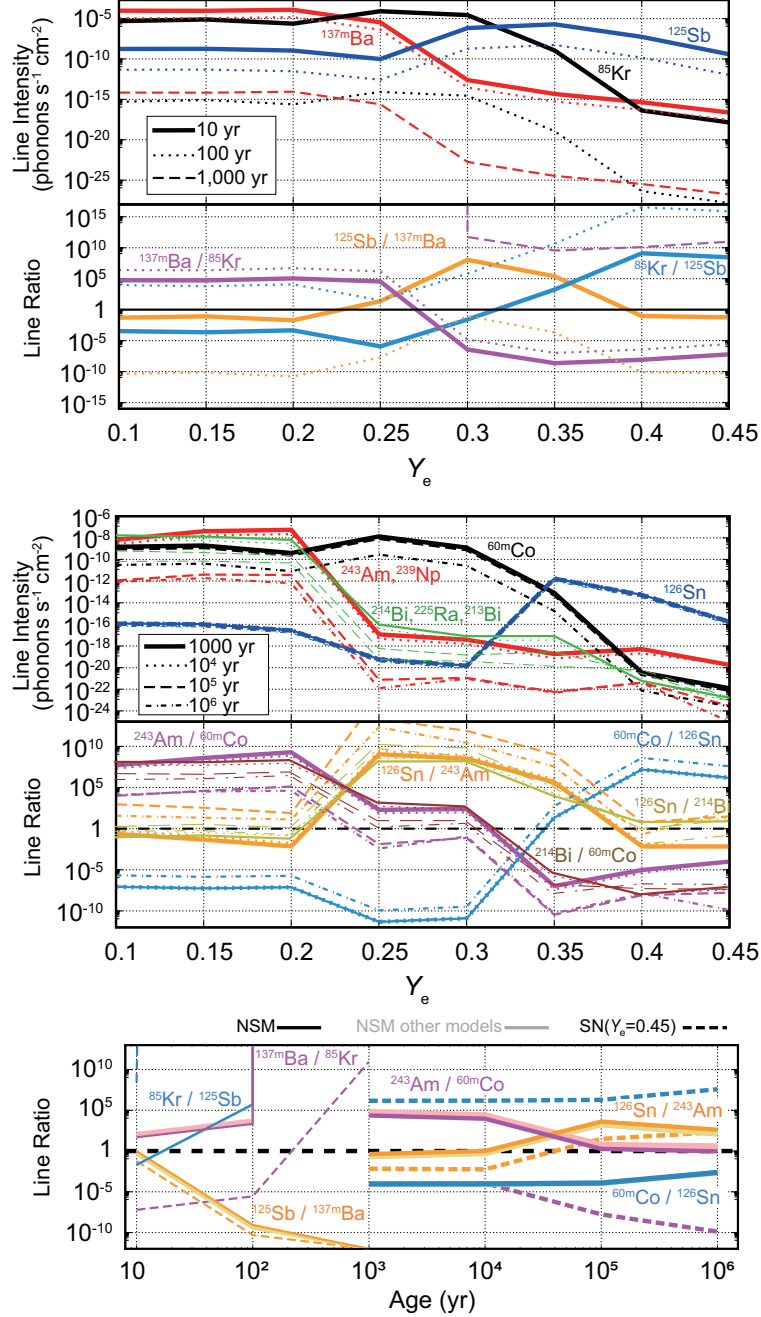


Figure 10. (Top) The Y_e dependencies of the line intensities of the nuclei listed with † marks in Table 1 are shown in the upper panel. The reduction due to the Doppler-broadening effect is not considered. The line intensities of ^{137m}Ba , ^{85}Kr , and ^{125}Sb are shown in red, black, and blue, respectively. Thick, dotted, and dashed lines represent the intensities at $t = 10$, 100 , and 1000 years. The ratios among the lines are plotted in the lower panel; the ratios between ^{137m}Ba and ^{85}Kr , ^{125}Sb and ^{137m}Ba , and ^{85}Kr and ^{125}Sb are shown in purple, orange, and cyan, respectively. (Middle) Same plot as the top panel but for older ages ($t > 100$ years, ‡ marks in Table 1). The dependencies of ^{243}Am (and ^{239}Np), ^{214}Bi (and ^{225}Ra , ^{213}Bi), ^{60m}Co , and ^{126}Sn are shown in red, green, black, and blue, respectively, and the thick, dotted, dashed, and dotted dash lines represent the intensity at $t = 1000$, 10^4 , 10^5 , and 10^6 years, respectively, in the upper panel. The ratios in the lower panel between ^{243}Am and ^{60m}Co , between ^{214}Bi and ^{60m}Co , between ^{126}Sn and ^{243}Am , between ^{126}Sn and ^{214}Bi , and between ^{60m}Co and ^{126}Sn are shown in purple, brown, orange, dark-yellow, and cyan, respectively. (Bottom) The time dependencies of the line ratios of $^{137m}Ba / ^{85}Kr$, $^{125}Sb / ^{137m}Ba$, $^{85}Kr / ^{125}Sb$, $^{243}Am / ^{60m}Co$, $^{126}Sn / ^{243}Am$, and $^{60m}Co / ^{126}Sn$ are shown in the thin purple, thin orange, thin cyan, thick purple, thick orange, and thick cyan lines, respectively. The NSM case by the mass fraction of Wanajo et al. (2014) and the case of $Y_e = 0.45$ are shown in the straight and dotted lines, respectively. The results by the other NSM models, DD2-125145, DD2-135135, SFHo-125145, and SFHo-135135 in Kullmann et al. (2022), are shown in the lighter colors.

astronomical objects up to $t = 10^5$ years old. Consequently, we can identify a γ -ray object as an NSM remnant using the γ -ray spectral colors (Section 3.1). Among the many nuclear lines in the spectra, we identified that the nuclear lines from ^{241}Am , ^{243}Am , ^{214}Pb , ^{239}Np , and ^{214}Bi are prominent for $t = 10^3$ – 10^4 years, and that the lines from ^{126}Sn and $^{126\text{m}}\text{Sb}$ are prominent for $t > 10^4$ years (Section 3.2). In addition, we proposed a new line-diagnostic method for distinguishing Y_e environments that uses the line ratios of $^{137\text{m}}\text{Ba}/^{85}\text{K}$ and $^{243}\text{Am}/^{60\text{m}}\text{Co}$, which become larger than unity for low Y_e objects with young and old ages, respectively (Section 3.3). This diagnostic method distinguishes NSMs from SNe. In the next section, we focus on the sensitivities in the γ -ray band that are required for current and future MeV γ -ray missions that aim to search for Galactic NSM remnants.

4.1. Detectable distance to Galactic Neutron-Star Merger Remnants

A γ -ray flux from the brightest line in a particular age range can be used to estimate the distance that a virtual γ -ray instrument with a certain line sensitivity will be able to detect. If we assume the age of the NSM remnants in Figure 9, then we can estimate the limit of the distance that can be detected with the line sensitivity of a specific instrument. The top of Figure 11 summarizes the achievable limit of d for NSM remnants as a function of t and is calculated for the three energy bands 3–75 keV, 75–500 keV, and 500–4,000 keV. For example, instruments with a line sensitivity of 10^{-7} photons $\text{s}^{-1} \text{cm}^{-2}$ in the 3–75 keV band (red line in the top of Figure 11), such as Hitomi HXI (Takahashi et al. 2014) and NuSTAR (Harrison et al. 2013), can observe the brightest lines from NSM remnants with $t < 10^3$ years at $d = 3$ kpc. We also checked the degradation of the distance limit due to the Doppler-broadening effect, as shown in the middle of Figure 11, but the results do not dramatically change. If the line sensitivities are the same among the three energy bands, then hard X-rays (thick lines) will be a powerful tool in the search for NSMs that are younger than $t < 10^3$ years, but the γ -ray observations (dotted or dashed lines) are better for surveying NSMs that are older than $t > 10^4$ years.

The G4.8+6.2 associated with AD 1163 is one example, from the middle of Figure 11, that provides the requirement for the γ -ray sensitivity needed to observe an NSM remnant with a known distance and age. The object is reported to be a young kilonova remnant with $t \sim 860$ years (Liu et al. 2019). If it is an NSM remnant at $d \sim 10$ kpc, then a sensitivity of 10^{-8} and 10^{-9} photons $\text{s}^{-1} \text{cm}^{-2}$ is required to observe G4.8+6.2 in the

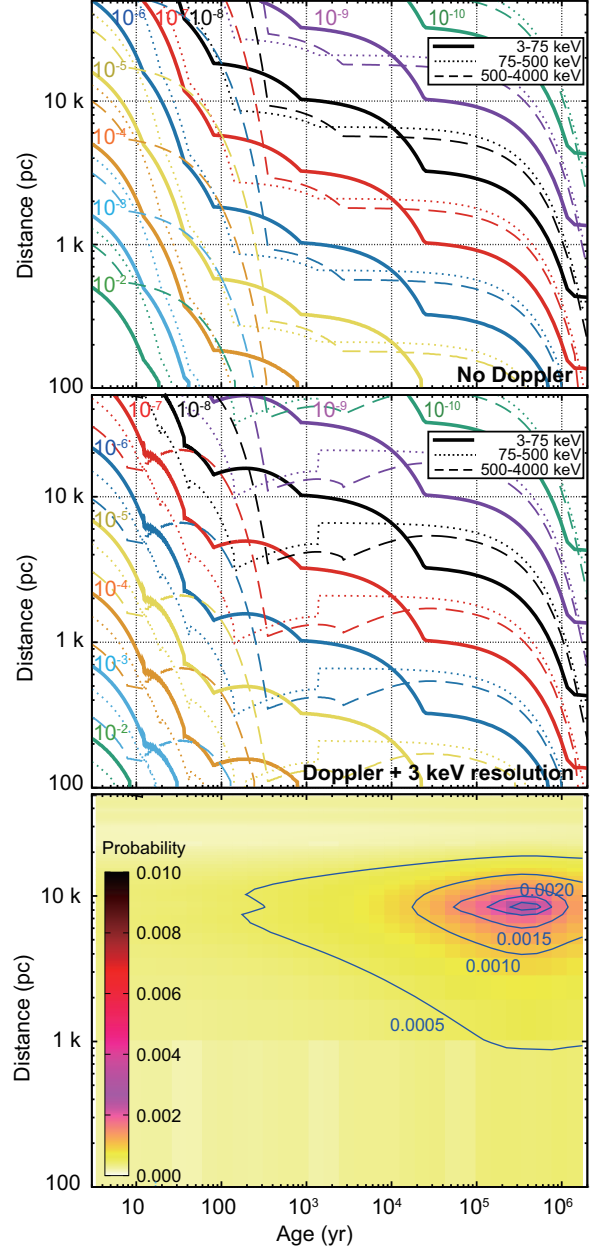


Figure 11. (Top, Middle) The distance limit of NSMs as a function of t are shown with the line sensitivities given in units of photons $\text{s}^{-1} \text{cm}^{-2}$; see keys for details. The thick, dotted, and dashed lines represent the results for the 3–75 keV, 75–500 keV, and 500–4,000 keV bands, respectively. The top and middle panels show the results without and with the Doppler-broadening effect, respectively. The line photons are accumulated within $\Delta E = 3$ keV in the middle panel. Note that the small jump in the 75–500 keV data at $t \sim 10^3$ years in the middle panel is due to the interaction between the two brightest lines when the Doppler-broadening effect is applied. (Bottom) Probabilities for the existence of NSMs, which we took as an assumption in the calculation for Figure 12, in the t – d plane.

hard X-ray and γ -ray bands, respectively. This sensitiv-

ity is roughly one or two (or more) orders of magnitude deeper than that of INTEGRAL IBIS (Winkler et al. 2003). If the distance is closer at $d \sim 3$ kpc, then hard X-ray instruments with a sensitivity of 10^{-7} photons $\text{s}^{-1} \text{cm}^{-2}$ in the 3–75 keV band, such as Hitomi HXI (Takahashi et al. 2014) and NuSTAR (Harrison et al. 2013), are expected to be able to observe the emissions from the object.

4.2. Direct estimation of local NSM rates using gamma rays

To estimate the coverage of Galactic NSM remnants observable for specific γ -ray sensitivities, we first prepare a probability map for the existence of Galactic NSMs. This is given in the same plane as the top and middle of Figure 11 (the t - d plane). Since NSMs are not uniformly distributed in our Galaxy, we apply the probabilities for NSMs in the d and t spaces given by Wu et al. (2019) and multiply them to get the plot shown in the bottom of Figure 11. We assume that the NSMs are primarily concentrated around the Galactic plane. Most of the NSMs are expected to exist at around $d \sim 8$ kpc and $t \sim 10^4$ – 10^6 years, as has already been described in Wu et al. (2019).

We then accumulate the probabilities for the existence of NSMs (bottom of Figure 11) within the distance-limit curves (top and middle of Figure 11). As a result, we obtained the coverage of Galactic NSMs as a function of the line sensitivity; this is shown in the top of Figure 12. For example, if we survey Galactic NSM remnants with an instrument having a line sensitivity of 10^{-8} photons $\text{s}^{-1} \text{cm}^{-2}$ in the 3–75 keV band, then we expect to observe about 3% of the NSMs in our Galaxy with $M_{\text{ej}} = 0.01 M_{\odot}$. This value corresponds to about one object if we assume an NSM rate in our Galaxy of 30 per million years. In addition, we performed the same procedure to estimate the NSM coverage in units of $\text{erg s}^{-1} \text{cm}^{-2}$, which requires a sensitivity that is E_{γ}^1 times higher than that required for units of photons $\text{s}^{-1} \text{cm}^{-2}$. E_{γ} here is the photon energy (the energy of the γ -ray line). The results are shown in the bottom of Figure 12. Therefore, instruments that can achieve a sensitivity of 10^{-14} $\text{erg s}^{-1} \text{cm}^{-2}$ in the 75–500 keV or the 500–4000 keV bands are expected to be able to observe one NSM remnant with $M_{\text{ej}} = 0.01 M_{\odot}$ in our Galaxy under the same assumption of the NSM rate mentioned above. Similarly, a sensitivity of 10^{-15} $\text{erg s}^{-1} \text{cm}^{-2}$ is required in the hard X-ray band to observe one object with the same M_{ej} .

The NSM rates from previous studies are summarized in Figure 13. The NSM rates are estimated using several methods, and even though the values approach each

other recently, they still have non-negligible uncertainties or systematic errors that are dependent on the methods used. According to Figure 12, instruments with higher sensitivities can cover more than 10% of NSMs and should be able to observe multiple Galactic NSM remnants (meaning a sensitivity of $10^{-9.5}$ – $10^{-8.5}$ photons $\text{s}^{-1} \text{cm}^{-2}$ or $10^{-16.5}$ – $10^{-14.5}$ $\text{erg s}^{-1} \text{cm}^{-2}$ in the hard X-ray to γ -ray bands). The actual numbers observed by future NSM surveys with highly sensitive in-

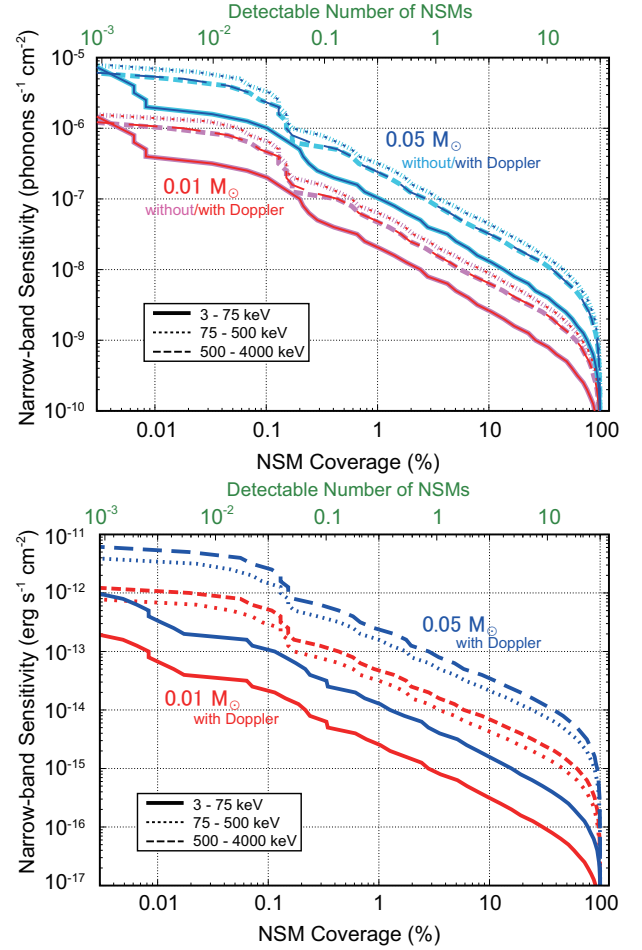


Figure 12. Coverage of NSM remnants in our Galaxy as a function of the narrow-band sensitivity is shown. In the top panel, the results are given in units of photons $\text{s}^{-1} \text{cm}^{-2}$. The magenta and red plots assume $M_{\text{ej}} = 0.01 M_{\odot}$ with and without the Doppler effect, respectively. Similarly, the cyan and blue plots assume $M_{\text{ej}} = 0.05 M_{\odot}$ with and without the Doppler effect. The thick, dotted, and dashed lines represent the coverage values in the 3–75 keV, 75–500 keV, and 500–4,000 keV bands, respectively. The top axis (shown in green) represents the detectable number of NSMs under the assumption of an NSM rate in our Galaxy of 30 per million years. The bottom panel shows the sensitivity results given in units of $\text{erg s}^{-1} \text{cm}^{-2}$, but omitting the results without the Doppler effect.

struments will provide direct information for the NSM rate in the local universe.

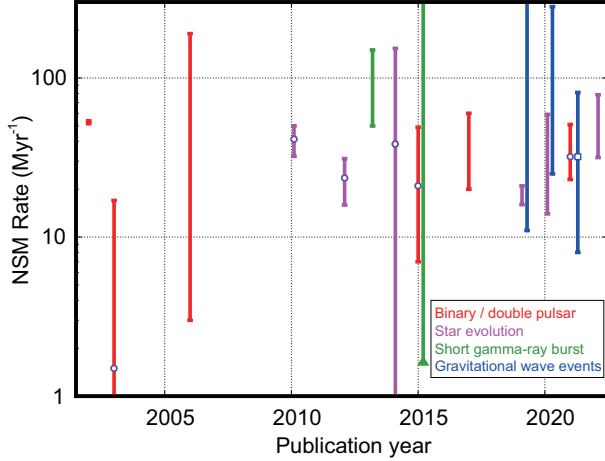


Figure 13. The NSM rate in our Galaxy estimated by previous studies as a function of the published year. The red, magenta, green, and blue plots represent the estimation from the binary or double pulsar population (Belczynski et al. 2002; Voss & Tauris 2003; Kim et al. 2006, 2015; Chruslinska et al. 2017; Pol et al. 2019; Grunthal et al. 2021), star evolution (Belczynski et al. 2010; Dominik et al. 2012; Mennekens & Vanbeveren 2014; Artale et al. 2019; Olejak et al. 2020; Chu et al. 2022), short gamma-ray bursts (Petrillo et al. 2013; Jin et al. 2015), and gravitational wave events (Abbott et al. 2019, 2020, 2021), respectively. The values from the gravitational wave events in $\text{Gpc}^{-3} \text{ yr}^{-1}$ are converted into the Myr^{-1} unit under the assumption of a galactic density of $0.01 \text{ galaxy Mpc}^{-3}$.

4.3. Sensitivity requirements for future missions

To assess the feasibility of detecting Galactic NSM remnants using past, current, and future γ -ray missions, the γ -ray spectra expected from NSMs (Figures 4 and 5) are compared with the sensitivities of the instruments for these missions in Figure 14. For the MeV bands, we expect that in the 2030s sensitivities will be achieved that are one or two orders of magnitude higher than those of current missions. Consequently, we conclude that future missions, such as e-ASTROGAM, AMEGO, and GRAMS, have the potential to detect MeV emissions from young NSM remnants in the age range of $t = 100\text{--}1000$ years old at 10 kpc, with a sensitivity of approximately $10^{-13}\text{--}10^{-11} \text{ erg cm}^{-2} \text{ s}^{-1}$. Furthermore, the hard X-ray band below 100 keV is also useful in searching for NSM remnants. NuSTAR data may be able to indicate very young NSM remnants at about $t = 100$ years, and FORCE may be able to detect emissions from an NSM older than $t < 10^4$ years at 10 kpc.

ACKNOWLEDGMENTS

This work was supported in part by JSPS KAKENHI [Grant Nos. JP18H04571 and JP20K04009 (YT), 18H01232 and 22H01251(RY), 20K03957 (SF), 20H00174 (SK), 21H01121 (SK, YT, SF), 19K03908 (AB)]. YT and SK are deeply appreciative of the Observational Astrophysics Institute at Saitama University for supporting the research fund, and R.Y. deeply appreciates the Aoyama Gakuin University Research Institute for helping to fund our research. Finally, we would like to thank the anonymous referee for his/her careful reading of our manuscript and helpful comments.

Facilities: INTEGRAL, CGRO, NuSTAR, Hitomi, Fermi, SMILE, GRAMS, AMEGO, e-ASTROGAM, FORCE

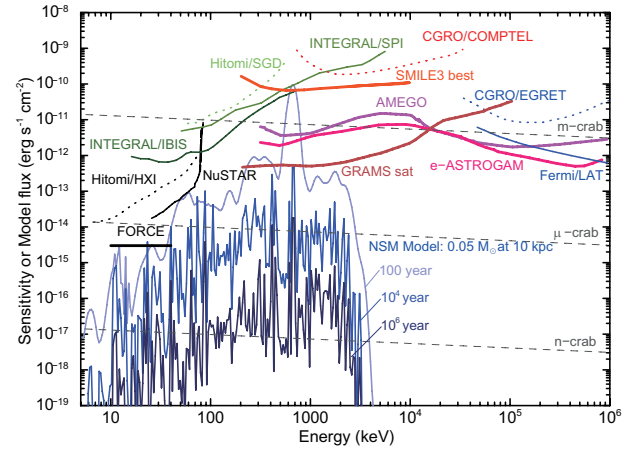


Figure 14. The 3σ sensitivities of the missions in the hard X-ray to γ -ray bands are compared with the γ rays expected from NSMs that are 100, 10^4 , and 10^6 years old, with the assumption of an ejecta mass of $0.05 M_{\odot}$ at a 10 kpc distance with $\Delta E = 3 \text{ keV}$. Past and future missions are shown with the dotted and thick lines, respectively. The sensitivities are taken from the following references: CGRO/COMPTEL (9 years), INTEGRAL/SPI (1 year), e-ASTROGAM (1 year), and Fermi LAT (10 years in survey mode) from de Angelis et al. (2018), INTEGRAL/IBIS (10^6 sec) and AMEGO (5 years) from Kierans (2020), CGRO/EGRET (9 years) from Si-liang et al. (2021), NuSTAR (10^6 sec) from Harrison et al. (2013), FORCE (3.5σ , 10^6 sec) from Nakazawa et al. (2018), Hitomi HXI and SGD (100 ksec) from Takahashi et al. (2014), SMILE3 (10^6 sec , best condition) from Takada et al. (2021), and GRAMS (1 year) from Aramaki et al. (2020). For reference, 1.0 , 10^{-3} , 10^{-6} , and 10^{-9} times the hard X-ray flux from the Crab Nebula (Kouzu et al. 2013), with a simple extension into the γ -ray band with the single power-law spectrum, are shown in dashed lines and are noted as m-crab, μ -crab, and n-crab, respectively.

REFERENCES

- Abbott, B. P., Abbott, R., Abbott, T. D., et al. 2017, *PhRvL*, 119, 161101, doi: [10.1103/PhysRevLett.119.161101](https://doi.org/10.1103/PhysRevLett.119.161101)
- . 2019, *Physical Review X*, 9, 031040, doi: [10.1103/PhysRevX.9.031040](https://doi.org/10.1103/PhysRevX.9.031040)
- . 2020, *ApJL*, 892, L3, doi: [10.3847/2041-8213/ab75f5](https://doi.org/10.3847/2041-8213/ab75f5)
- Abbott, R., Abbott, T. D., Abraham, S., et al. 2021, *ApJL*, 913, L7, doi: [10.3847/2041-8213/abe949](https://doi.org/10.3847/2041-8213/abe949)
- Andrews, S., Fryer, C., Even, W., Jones, S., & Pignatari, M. 2020, *ApJ*, 890, 35, doi: [10.3847/1538-4357/ab64f8](https://doi.org/10.3847/1538-4357/ab64f8)
- Aramaki, T., Adrian, P. O. H., Karagiorgi, G., & Odaka, H. 2020, *Astroparticle Physics*, 114, 107, doi: [10.1016/j.astropartphys.2019.07.002](https://doi.org/10.1016/j.astropartphys.2019.07.002)
- Arnaud, K. A. 1996, in *Astronomical Society of the Pacific Conference Series*, Vol. 101, *Astronomical Data Analysis Software and Systems V*, ed. G. H. Jacoby & J. Barnes, 17
- Arnould, M., Goriely, S., & Takahashi, K. 2007, *PhR*, 450, 97, doi: [10.1016/j.physrep.2007.06.002](https://doi.org/10.1016/j.physrep.2007.06.002)
- Artale, M. C., Mapelli, M., Giacobbo, N., et al. 2019, *MNRAS*, 487, 1675, doi: [10.1093/mnras/stz1382](https://doi.org/10.1093/mnras/stz1382)
- Beer, H., Corvi, F., & Mutti, P. 1997, *ApJ*, 474, 843, doi: [10.1086/303480](https://doi.org/10.1086/303480)
- Belczynski, K., Dominik, M., Bulik, T., et al. 2010, *ApJL*, 715, L138, doi: [10.1088/2041-8205/715/2/L138](https://doi.org/10.1088/2041-8205/715/2/L138)
- Belczynski, K., Kalogera, V., & Bulik, T. 2002, *ApJ*, 572, 407, doi: [10.1086/340304](https://doi.org/10.1086/340304)
- Burbidge, E. M., Burbidge, G. R., Fowler, W. A., & Hoyle, F. 1957, *Reviews of Modern Physics*, 29, 547, doi: [10.1103/RevModPhys.29.547](https://doi.org/10.1103/RevModPhys.29.547)
- Cameron, A. G. W. 1957, *PASP*, 69, 201, doi: [10.1086/127051](https://doi.org/10.1086/127051)
- Chruslinska, M., Belczynski, K., Bulik, T., & Gladysz, W. 2017, *AcA*, 67, 37, doi: [10.32023/0001-5237/67.1.2](https://doi.org/10.32023/0001-5237/67.1.2)
- Chu, Q., Yu, S., & Lu, Y. 2022, *MNRAS*, 509, 1557, doi: [10.1093/mnras/stab2882](https://doi.org/10.1093/mnras/stab2882)
- Cowan, J. J., Thielemann, F.-K., & Truran, J. W. 1991, *PhR*, 208, 267, doi: [10.1016/0370-1573\(91\)90070-3](https://doi.org/10.1016/0370-1573(91)90070-3)
- De Angelis, A., Tatischeff, V., Tavani, M., et al. 2017, *Experimental Astronomy*, 44, 25, doi: [10.1007/s10686-017-9533-6](https://doi.org/10.1007/s10686-017-9533-6)
- de Angelis, A., Tatischeff, V., Grenier, I. A., et al. 2018, *Journal of High Energy Astrophysics*, 19, 1, doi: [10.1016/j.jheap.2018.07.001](https://doi.org/10.1016/j.jheap.2018.07.001)
- Dominik, M., Belczynski, K., Fryer, C., et al. 2012, *ApJ*, 759, 52, doi: [10.1088/0004-637X/759/1/52](https://doi.org/10.1088/0004-637X/759/1/52)
- Freiburghaus, C., Rosswog, S., & Thielemann, F. K. 1999, *ApJL*, 525, L121, doi: [10.1086/312343](https://doi.org/10.1086/312343)
- Fujimoto, S.-i., Hashimoto, M.-a., Kotake, K., & Yamada, S. 2007, *ApJ*, 656, 382, doi: [10.1086/509908](https://doi.org/10.1086/509908)
- Grefenstette, B. W., Fryer, C. L., Harrison, F. A., et al. 2017, *ApJ*, 834, 19, doi: [10.3847/1538-4357/834/1/19](https://doi.org/10.3847/1538-4357/834/1/19)
- Grunthal, K., Kramer, M., & Desvignes, G. 2021, *MNRAS*, 507, 5658, doi: [10.1093/mnras/stab2198](https://doi.org/10.1093/mnras/stab2198)
- Hanisch, R. J., Farris, A., Greisen, E. W., et al. 2001, *A&A*, 376, 359, doi: [10.1051/0004-6361:20010923](https://doi.org/10.1051/0004-6361:20010923)
- Harrison, F. A., Craig, W. W., Christensen, F. E., et al. 2013, *ApJ*, 770, 103, doi: [10.1088/0004-637X/770/2/103](https://doi.org/10.1088/0004-637X/770/2/103)
- Hempel, M., & Schaffner-Bielich, J. 2010, *NuPhA*, 837, 210, doi: [10.1016/j.nuclphysa.2010.02.010](https://doi.org/10.1016/j.nuclphysa.2010.02.010)
- Hotokezaka, K., Piran, T., & Paul, M. 2015, *Nature Physics*, 11, 1042, doi: [10.1038/nphys3574](https://doi.org/10.1038/nphys3574)
- Hotokezaka, K., Wanajo, S., Tanaka, M., et al. 2016, *MNRAS*, 459, 35, doi: [10.1093/mnras/stw404](https://doi.org/10.1093/mnras/stw404)
- Jin, Z.-P., Li, X., Cano, Z., et al. 2015, *ApJL*, 811, L22, doi: [10.1088/2041-8205/811/2/L22](https://doi.org/10.1088/2041-8205/811/2/L22)
- Kasuga, T., Sato, T., Mori, K., Yamaguchi, H., & Bamba, A. 2018, *PASJ*, 70, 88, doi: [10.1093/pasj/psy085](https://doi.org/10.1093/pasj/psy085)
- Katakura, J. 2012, *JAEA-Data/Code*, 2011-025
- Katakura, J., & Minato, F. 2016, *JAEA-Data/Code*, 2015-030
- Kierans, C. A. 2020, in *Society of Photo-Optical Instrumentation Engineers (SPIE) Conference Series*, Vol. 11444, *Society of Photo-Optical Instrumentation Engineers (SPIE) Conference Series*, 1144431, doi: [10.1117/12.2562352](https://doi.org/10.1117/12.2562352)
- Kim, C., Kalogera, V., & Lorimer, D. R. 2006, *arXiv e-prints*, astro. <https://arxiv.org/abs/astro-ph/0608280>
- Kim, C., Perera, B. B. P., & McLaughlin, M. A. 2015, *MNRAS*, 448, 928, doi: [10.1093/mnras/stu2729](https://doi.org/10.1093/mnras/stu2729)
- Kouzu, T., Tashiro, M. S., Terada, Y., et al. 2013, *PASJ*, 65, 74, doi: [10.1093/pasj/65.4.74](https://doi.org/10.1093/pasj/65.4.74)
- Kullmann, I., Goriely, S., Just, O., et al. 2022, *MNRAS*, 510, 2804, doi: [10.1093/mnras/stab3393](https://doi.org/10.1093/mnras/stab3393)
- Lattimer, J. M., & Schramm, D. N. 1974, *ApJL*, 192, L145, doi: [10.1086/181612](https://doi.org/10.1086/181612)
- Li, L.-X. 2019, *ApJ*, 872, 19, doi: [10.3847/1538-4357/aaf961](https://doi.org/10.3847/1538-4357/aaf961)
- Liu, Y., Zou, Y.-C., Jiang, B., et al. 2019, *MNRAS*, 490, L21, doi: [10.1093/mnrasl/slz141](https://doi.org/10.1093/mnrasl/slz141)
- McKee, C. F., & Ostriker, J. P. 1977, *ApJ*, 218, 148, doi: [10.1086/155667](https://doi.org/10.1086/155667)
- Mennekens, N., & Vanbeveren, D. 2014, *A&A*, 564, A134, doi: [10.1051/0004-6361/201322198](https://doi.org/10.1051/0004-6361/201322198)
- Metzger, B. D., Martínez-Pinedo, G., Darbha, S., et al. 2010, *MNRAS*, 406, 2650, doi: [10.1111/j.1365-2966.2010.16864.x](https://doi.org/10.1111/j.1365-2966.2010.16864.x)

- Nakazawa, K., Mori, K., Tsuru, T. G., et al. 2018, in Society of Photo-Optical Instrumentation Engineers (SPIE) Conference Series, Vol. 10699, Space Telescopes and Instrumentation 2018: Ultraviolet to Gamma Ray, ed. J.-W. A. den Herder, S. Nikzad, & K. Nakazawa, 106992D, doi: [10.1117/12.2309344](https://doi.org/10.1117/12.2309344)
- Olejak, A., Belczynski, K., Bulik, T., & Sobolewska, M. 2020, *A&A*, 638, A94, doi: [10.1051/0004-6361/201936557](https://doi.org/10.1051/0004-6361/201936557)
- Petrillo, C. E., Dietz, A., & Cavaglià, M. 2013, *ApJ*, 767, 140, doi: [10.1088/0004-637X/767/2/140](https://doi.org/10.1088/0004-637X/767/2/140)
- Pol, N., McLaughlin, M., & Lorimer, D. R. 2019, *ApJ*, 870, 71, doi: [10.3847/1538-4357/aaf006](https://doi.org/10.3847/1538-4357/aaf006)
- Qian, Y. Z., & Wasserburg, G. J. 2007, *PhR*, 442, 237, doi: [10.1016/j.physrep.2007.02.006](https://doi.org/10.1016/j.physrep.2007.02.006)
- Si-liang, F., Peng, F., Yi-fan, H., Tian-yu, M., & Yan, X. 2021, *ChA&A*, 45, 281, doi: [10.1016/j.chinastron.2021.08.002](https://doi.org/10.1016/j.chinastron.2021.08.002)
- Steiner, A. W., Hempel, M., & Fischer, T. 2013, *ApJ*, 774, 17, doi: [10.1088/0004-637X/774/1/17](https://doi.org/10.1088/0004-637X/774/1/17)
- Takada, A., Takemura, T., Yoshikawa, K., et al. 2021, arXiv e-prints, arXiv:2107.00180. <https://arxiv.org/abs/2107.00180>
- Takahashi, T., Mitsuda, K., Kelley, R., et al. 2014, in Society of Photo-Optical Instrumentation Engineers (SPIE) Conference Series, Vol. 9144, Space Telescopes and Instrumentation 2014: Ultraviolet to Gamma Ray, ed. T. Takahashi, J.-W. A. den Herder, & M. Bautz, 914425, doi: [10.1117/12.2055681](https://doi.org/10.1117/12.2055681)
- Tanvir, N. R., Levan, A. J., Fruchter, A. S., et al. 2013, *Nature*, 500, 547, doi: [10.1038/nature12505](https://doi.org/10.1038/nature12505)
- Taylor, G. 1950, Proceedings of the Royal Society of London Series A, 201, 159, doi: [10.1098/rspa.1950.0049](https://doi.org/10.1098/rspa.1950.0049)
- Typel, S., Röpke, G., Klähn, T., Blaschke, D., & Wolter, H. H. 2010, *PhRvC*, 81, 015803, doi: [10.1103/PhysRevC.81.015803](https://doi.org/10.1103/PhysRevC.81.015803)
- Villar, V. A., Guillochon, J., Berger, E., et al. 2017, *ApJL*, 851, L21, doi: [10.3847/2041-8213/aa9c84](https://doi.org/10.3847/2041-8213/aa9c84)
- Voss, R., & Tauris, T. M. 2003, *MNRAS*, 342, 1169, doi: [10.1046/j.1365-8711.2003.06616.x](https://doi.org/10.1046/j.1365-8711.2003.06616.x)
- Wallner, A., Faestermann, T., Feige, J., et al. 2015, *Nature Communications*, 6, 5956, doi: [10.1038/ncomms6956](https://doi.org/10.1038/ncomms6956)
- Wanajo, S., & Ishimaru, Y. 2006, *NuPhA*, 777, 676, doi: [10.1016/j.nuclphysa.2005.10.012](https://doi.org/10.1016/j.nuclphysa.2005.10.012)
- Wanajo, S., Janka, H.-T., & Müller, B. 2011, *ApJL*, 726, L15, doi: [10.1088/2041-8205/726/2/L15](https://doi.org/10.1088/2041-8205/726/2/L15)
- Wanajo, S., Sekiguchi, Y., Nishimura, N., et al. 2014, *ApJL*, 789, L39, doi: [10.1088/2041-8205/789/2/L39](https://doi.org/10.1088/2041-8205/789/2/L39)
- Wang, X., N3AS Collaboration, Vassh, N., et al. 2020, *ApJL*, 903, L3, doi: [10.3847/2041-8213/abbe18](https://doi.org/10.3847/2041-8213/abbe18)
- Winkler, C., Courvoisier, T. J. L., Di Cocco, G., et al. 2003, *A&A*, 411, L1, doi: [10.1051/0004-6361:20031288](https://doi.org/10.1051/0004-6361:20031288)
- Wu, M.-R., Banerjee, P., Metzger, B. D., et al. 2019, *ApJ*, 880, 23, doi: [10.3847/1538-4357/ab2593](https://doi.org/10.3847/1538-4357/ab2593)

